

Mimicking acceleration in the constant-bang-time Lemaître – Tolman model: Shell crossings, density distributions and light cones

Andrzej Krasiński

*N. Copernicus Astronomical Centre,
Polish Academy of Sciences,
Bartycka 18, 00 716 Warszawa, Poland**

(Dated:)

The Lemaître – Tolman model with $\Lambda = 0$ and constant bang time that imitates the luminosity distance – redshift relation of the Λ CDM model using the energy function E alone contains shell crossings. In this paper, the location in spacetime and the consequences of existence of the shell-crossing set (SCS) are investigated. The SCS would come into view of the central observer only at $t \approx 1064T$ to the future from now, where T is the present age of the Universe, but would not leave any recognizable trace in her observations. Light rays emitted near to the SCS are blueshifted at the initial points, but the blueshift is finite, and is overcompensated by later-induced redshifts if the observer is sufficiently far. The local blueshifts cause that z along a light ray is not a monotonic function of the comoving radial coordinate r . As a consequence, the angular diameter distance D_A and the luminosity distance D_L from the central observer fail to be functions of z ; the relations $D_A(z)$ and $D_L(z)$ are multiple-valued in a vicinity of the SCS. The following quantities are calculated and displayed: (1) The distribution of mass density on a few characteristic hypersurfaces of constant time; some of them intersect the SCS. (2) The distribution of density along the past light cone of the present central observer. (3) A few light cones intersecting the SCS at characteristic instants. (4) The redshift profiles along several light cones. (5) The extremum-redshift hypersurface. (6) The $D_A(z)$ and $D_L(z)$ relations. (7) The last scattering time and its comparison with the Λ CDM last scattering epoch.

PACS numbers:
Keywords:

I. MOTIVATION AND OVERVIEW

In Ref. [1] it was shown how the luminosity distance – redshift relation $D_L(z)$ of the Λ CDM model is duplicated in the Lemaître [2] – Tolman [3] (L–T) model with $\Lambda = 0$, constant bang-time function t_B and the energy function E mimicking accelerated expansion on the past light cone of the present central observer (PCPO). This model was first introduced in Ref. [4], and further investigated in Ref. [5]. Numerical calculations in Ref. [1] revealed that this model necessarily contains shell crossings in the region whose boundary intersects the PCPO at $z = z_{sc} \approx 6.938$. This is far enough to avoid any problems with the observations of the type Ia supernovae [6–8], the farthest of which are at $z_{far} = 1.914$ [8]. The shell crossings can be removed from the model by matching it to a background (Friedmann, for example), at the radial coordinate $r = r_m$, where the redshift corresponding to r_m at the PCPO is smaller than z_{sc} , but larger than z_{far} [1].

In the present paper, the position of the shell-crossing set (SCS) relative to the PCPO in that L–T model, and the consequences of its existence, are investigated. The SCS lies so far to the future of the present time that it has no influence on any observations that the present central observer could have carried out until now (see below). Consequently, even if not removed, the shell crossing is

invisible for her. However, the position of the SCS in spacetime is a consequence of the values of parameters of this particular model. With a different shape of the $E(r)$ function, perhaps even with different values of the Ω parameters, the SCS might appear early enough to be visible to the present observer. In such a model, the findings about the redshift profiles presented here will become relevant for the present-day astrophysics.

Sections II and III provide the basic formulae for reference, extracted from Ref. [1]. In Sec. IV, the profile and properties of the PCPO are presented. The location of the SCS in spacetime is determined in Sec. V.

In Sec. VI, the distributions of mass density on a few characteristic hypersurfaces of constant time are displayed; some of them intersect the SCS. The distribution at the present time is, in agreement with common expectation [9, 10], that of a void, but with a cusp rather than a smooth minimum at the center.¹ In Sec. VII, the distribution of density along the PCPO is displayed.

In Sec. VIII, the earliest ray emitted at the SCS that will reach the central observer is determined. The observer will receive it at approximately $1064 T$ in the future, where $T = 13.819 \times 10^9$ y is the observationally determined present age of the Universe [13]. Two other light cones that intersect the SCS are calculated and dis-

*Electronic address: akr@camk.edu.pl

¹ In some papers [11] such a cusp was (mis)named a “weak singularity”, although in truth there is no singularity there [12].

played. As expected, in the comoving coordinates they are horizontal at the intersection points.

In Sec. IX, redshift profiles along several past light cones reaching the central observer are displayed. It is noted that on rays passing near the SCS the function $z(r)$ has a local maximum at a certain r and becomes decreasing for larger r . This means that rays emitted near or at the SCS are blueshifted at the initial points, but the blueshifts are finite and are overcompensated by redshifts accumulated later along the ray. At the intersection of a light cone with the SCS, the redshift profile has no recognizable mark.

In Sec. X, the location of the extremum-redshift hypersurface (ERH) in spacetime is determined and displayed. (Along some rays, the maximum of $z(r)$ is followed by a minimum. The maxima and minima lie on the ERH.) In Sec. XI, the relations $D_A(z)$ and $D_L(z)$ are displayed, where D_A and D_L are the angular-diameter distance and luminosity distance from the central observer. These relations become double- or even triple-valued in the blueshift-generating region.

In Sec. XII, the timing of the last scattering in the L-T model discussed here is compared to that in the Λ CDM model. The time difference is small and finds a neat intuitive explanation.

Section XIII presents the final summary of the results.

II. BASIC FORMULAE

This is a brief summary of basic facts about the L-T model, included here mainly in order to define the notation and conventions. For extended expositions see Refs. [14, 15].

The metric of the model considered here is

$$ds^2 = dt^2 - \frac{R_{,r}^2}{1+2E(r)} dr^2 - R^2(t,r)(d\vartheta^2 + \sin^2\vartheta d\varphi^2), \quad (2.1)$$

where $E(r)$ is an arbitrary function, and $R(t,r)$ obeys

$$R_{,t}^2 = 2E(r) + 2M(r)/R, \quad (2.2)$$

with $M(r)$ being another arbitrary function.

In the present paper, only the case $E > 0$ will be considered. Then the solution of (2.2) is

$$\begin{aligned} R(t,r) &= \frac{M}{2E}(\cosh\eta - 1), \\ \sinh\eta - \eta &= \frac{(2E)^{3/2}}{M}[t - t_B(r)]. \end{aligned} \quad (2.3)$$

The function $t_B(r)$ is constant in the model considered here. The r -coordinate is chosen so that

$$M = M_0 r^3, \quad (2.4)$$

and the remaining freedom of rescaling r is used to take $M_0 = 1$ in numerical calculations. The pressure is zero,

and the mass density is

$$\kappa\rho = \frac{2M_{,r}}{R^2 R_{,r}}, \quad \kappa \stackrel{\text{def}}{=} \frac{8\pi G}{c^2}. \quad (2.5)$$

Past radial null geodesics obey the equation

$$\frac{dt}{dr} = -\frac{R_{,r}}{\sqrt{1+2E(r)}}. \quad (2.6)$$

The redshifts $z(r)$ of the light sources lying along this light cone obey [16], [14]

$$\frac{1}{1+z} \frac{dz}{dr} = \left[\frac{R_{,tr}}{\sqrt{1+2E}} \right]_{\text{ng}}. \quad (2.7)$$

The luminosity distance between the central observer and the light sources lying along $t_{\text{ng}}(r)$ is

$$D_L(z) = (1+z)^2 R(t_{\text{ng}}(r), r). \quad (2.8)$$

The particular solution of (2.2) considered in this paper arose from the requirement that the $D_L(z)$ given above coincides with that calculated from the Λ CDM model,

$$D_L(z) = \frac{1+z}{H_0} \int_0^z \frac{dz'}{\sqrt{\Omega_m(1+z')^3 + \Omega_\Lambda}}, \quad (2.9)$$

where H_0 is the value of the Hubble parameter at the present time. It is related to the Hubble constant [13]

$$\mathcal{H}_0 = 67.1 \text{ km}/(\text{s} \times \text{Mpc}) \quad (2.10)$$

by

$$H_0 = \mathcal{H}_0/c. \quad (2.11)$$

The two dimensionless parameters

$$(\Omega_m, \Omega_\Lambda) \stackrel{\text{def}}{=} \frac{1}{3H_0^2} \left(\frac{8\pi G\rho_0}{c^2}, -\Lambda \right) \Big|_{t=t_0} \quad (2.12)$$

obey $\Omega_m + \Omega_\Lambda \equiv 1$; ρ_0 is the present mean mass density in the Universe. Their values

$$(\Omega_m, \Omega_\Lambda) = (0.32, 0.68) \quad (2.13)$$

also come from observations [13].

The requirement that the two expressions for $D_L(z)$, (2.8) and (2.9), are equal along the radial null geodesic reaching the central observer by now determines the functions $E(r)$, $t = t_{\text{ng}}(r)$ obeying (2.6) and $z(r)$ obeying (2.7). They were numerically calculated in Ref. [1] (see Sec. IV, Fig. 2 for $E(r)$ and Fig. 1 for $t_{\text{ng}}(r)$).

The apparent horizon (AH) of the central observer is a locus where R , calculated along the null geodesic given by (2.6), changes from increasing to decreasing, i.e., where $(d/dr)R(t_{\text{ng}}(r), r) = 0$. With $\Lambda = 0$, the general equation implicitly determining the function $t(r)$ along the AH is

$$R(t, r) = 2M(r). \quad (2.14)$$

In the model considered here, the values of r and z at the intersection of the PCPO with the AH are [1]²

$$r_{\text{AH}} = 0.3105427968086945, \quad (2.15)$$

$$z_{\text{AH}} = 1.582430687623614. \quad (2.16)$$

Since we consider here an L-T model with constant t_B , light emitted at the Big Bang (BB) will be infinitely redshifted, as in the Robertson – Walker (RW) models [17], [18], [14].

The numerical units used here were introduced in Ref. [19]. They are the numerical length unit (NLU) = the numerical time unit (NTU) related to the usual units by

$$\begin{aligned} 1 \text{ NTU} &= 1 \text{ NLU} = 3 \times 10^4 \text{ Mpc} \\ &= 9.26 \times 10^{23} \text{ km} = 9.8 \times 10^{10} \text{ y}. \end{aligned} \quad (2.17)$$

In the above,

$$c \approx 3 \times 10^5 \text{ km/s} \quad (2.18)$$

was taken for the speed of light, and the following values of the conversion factors were used [20]:

$$\begin{aligned} 1 \text{ pc} &= 3.086 \times 10^{13} \text{ km}, \\ 1 \text{ y} &= 3.156 \times 10^7 \text{ s} \end{aligned} \quad (2.19)$$

In these units

$$H_0 = 6.71 \text{ (NLU)}^{-1}, \quad (2.20)$$

$$T = 13.819 \times 10^9 \text{ y} = 0.141 \text{ NTU}, \quad (2.21)$$

where T is the age of the Λ CDM Universe [13].

The age in the model used here is somewhat different:

$$T_{\text{model}} = -t_B = 0.1329433206844743 \text{ NTU}. \quad (2.22)$$

The mass associated to $M_0 = 1 \text{ NLU}$ in (2.4) is

$$m_0 \approx 1.5 \times 10^{54} \text{ kg}, \quad (2.23)$$

but it will appear only via M_0 . The value of the gravitational constant used in numerical calculations is [21]

$$G = 6.674 \times 10^{-11} \text{ m}^3/(\text{kg} \times \text{s}^2). \quad (2.24)$$

III. USEFUL FORMULAE FOR NUMERICAL CALCULATIONS

With $t_B = \text{constant}$ and M given by (2.4) we have [14]

$$R_{,r} = \left(\frac{3}{r} - \frac{E_{,r}}{E} \right) R + \left(\frac{3}{2} \frac{E_{,r}}{E} - \frac{3}{r} \right) (t - t_B) R_{,t}. \quad (3.1)$$

In order to avoid a permanent singularity at the center of symmetry, the function E must be of the form [14]

$$2E(r) = r^2[-k + \mathcal{F}(r)], \quad (3.2)$$

where $\mathcal{F}(r)$ must obey

$$\lim_{r \rightarrow 0} \mathcal{F} = 0, \quad (3.3)$$

and the constant k was determined in Ref. [1]:

$$k = -21.916458. \quad (3.4)$$

Substituting (2.4) and (3.2) in (2.3) we obtain

$$R = \frac{M_0 r}{-k + \mathcal{F}} (\cosh \eta - 1), \quad (3.5)$$

$$\sinh \eta - \eta = \frac{(-k + \mathcal{F})^{3/2}}{M_0} (t - t_B). \quad (3.6)$$

Equations (3.5) – (3.6) determine $R(t, r)$. The function $\mathcal{F}(r)$ was numerically determined in Ref. [1].

From (3.1) and (2.7), using (2.2) and (3.2), we find:

$$\begin{aligned} \frac{dz}{dr} &= \frac{1+z}{\sqrt{1+r^2(-k+\mathcal{F})}} \\ &\times \left\{ \left[1 + \frac{r\mathcal{F}_{,r}}{2(-k+\mathcal{F})} \right] \sqrt{-k+\mathcal{F}} \sqrt{\frac{\cosh \eta + 1}{\cosh \eta - 1}} \right. \\ &\quad \left. - \frac{3}{2} \frac{r\mathcal{F}_{,r}(-k+\mathcal{F})}{M_0(\cosh \eta - 1)^2} (t - t_B) \right\}. \end{aligned} \quad (3.7)$$

The limit $r \rightarrow 0$ of this is, using (3.3) and (3.6),

$$\frac{dz}{dr}(0) = \sqrt{-k} \left. \sqrt{\frac{\cosh \eta + 1}{\cosh \eta - 1}} \right|_{r=0}, \quad (3.8)$$

where $\eta_0 \stackrel{\text{def}}{=} \eta|_{r=0}$ is found by solving (3.6) at $r = 0$.

Since t_B is given by (2.22), and the function $\mathcal{F}(r)$ is given as a numerical table, the solution of (2.14) can be numerically found in the form $t = t_{\text{AH}}(r)$ from (3.6), with $\eta(r)$ along the AH being found from (3.5) as follows:

$$\eta_{\text{AH}}(r) = \ln \left[x(r) + \sqrt{x^2(r) - 1} \right], \quad (3.9)$$

where

$$x(r) \stackrel{\text{def}}{=} 1 + 2r^2(-k + \mathcal{F}). \quad (3.10)$$

Substituting (3.2), (3.5) and (3.6) in (3.1) we obtain

$$\begin{aligned} R_{,r} &= \left(1 - \frac{r\mathcal{F}_{,r}}{-k+\mathcal{F}} \right) \frac{M_0}{-k+\mathcal{F}} (\cosh \eta - 1) \\ &+ \frac{3}{2} \frac{r\mathcal{F}_{,r}}{\sqrt{-k+\mathcal{F}}} (t - t_B) \sqrt{\frac{\cosh \eta + 1}{\cosh \eta - 1}}. \end{aligned} \quad (3.11)$$

The limit $r \rightarrow 0$ of this is

$$R_{,r}(t, 0) = \frac{M_0}{(-k)} (\cosh \eta_0 - 1). \quad (3.12)$$

² The numbers calculated for this paper by Fortran 90 are all at double precision – to minimise misalignments in the graphs.

IV. THE PAST LIGHT CONE OF THE PRESENT CENTRAL OBSERVER

To calculate the PCPO, $z(r)$ had to be calculated first. Since $z \rightarrow \infty$ at the BB, the numerical calculation broke down at $r = r_{\max}$, with $z = z_{\max}$, where [1]

$$\begin{pmatrix} r_{\max} \\ z_{\max} \end{pmatrix} = \begin{pmatrix} 1.045516839812362 \\ 9.1148372886058313 \times 10^{225} \end{pmatrix}. \quad (4.1)$$

The model extends from the center of symmetry up to that flow line, at which the PCPO reaches the BB. In practice this is the flow line corresponding to the r_{\max} given above. For $r > r_{\max}$, the model is not determined. Extensions into the range $r > r_{\max}$ are possible, but are not constrained by (2.9), and are not considered here.

The numerically calculated profile $t(r)$ of the PCPO is reproduced in Fig. 1 (from Ref. [1]), together with the profile of the AH calculated from (3.6) and (3.9) – (3.10). The two profiles intersect at the point $(r, t) = (r_{\text{AH}}, t_{\text{AH}})$, where r_{AH} is given by (2.15) and [1]

$$t_{\text{AH}} = -0.0966669255756665 \text{ NTU}. \quad (4.2)$$

The inset in Fig. 1 shows the AH up to the edge of the model. The last point on it has the coordinates

$$\begin{pmatrix} r_{\text{edge}} \\ t_{\text{edge}} \end{pmatrix} = \begin{pmatrix} 1.0455189100976430 \\ 1.2308128894377963 \end{pmatrix}. \quad (4.3)$$

This explains why the AH will not be seen in the graphs corresponding to late times (see next sections).

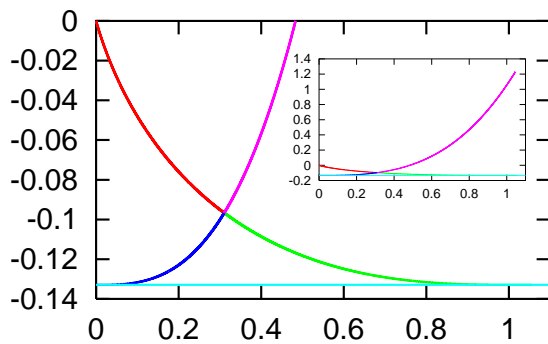


FIG. 1: The profiles $t(r)$ of the past light cone of the present central observer (the decreasing curve) and of the apparent horizon (the increasing curve). The horizontal line is $t = t_B$. The inset shows the AH in the full range of r .

V. THE SHELL CROSSINGS

The shell crossing is a locus, where $R_{,r} = 0$ while $M_{,r} \neq 0$. As seen from (2.5), this is a curvature singularity, at which the mass density becomes infinite, and changes sign if $R_{,r}$ does. When $t_B = \text{constant}$ and $E > 0$, the necessary and sufficient condition for the absence of shell

crossings is $E_{,r} > 0$. However, the $E(r)$ calculated in Ref. [1], shown in Fig. 2, has a maximum at

$$r = r_{\text{sc}} = 0.6293128978680214, \quad (5.1)$$

and becomes decreasing for $r > r_{\text{sc}}$. Thus, there are shell crossings in the region $r > r_{\text{sc}}$. The location of the SCS was not determined in Ref. [1], and we shall do it here.

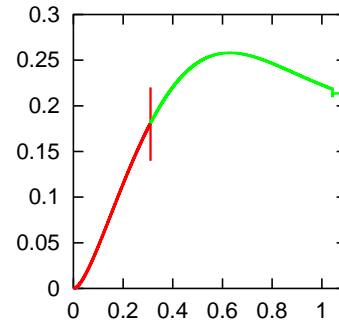


FIG. 2: The function $E(r)$ in the present model. The irregular segment at the right end is caused by numerical fluctuations in the neighbourhood of the Big Bang. The vertical stroke is at $r = r_{\text{AH}}$. Since $E(r)$ becomes decreasing for $r > r_{\text{sc}}$, given by (5.1), there are shell crossings in that region.

The equation $R_{,r} = 0$, using (3.11), can be written as

$$\frac{1}{r} + \frac{\mathcal{F}_{,r}}{-k + \mathcal{F}} \left[\frac{3}{2} Q(\eta) - 1 \right] = 0, \quad (5.2)$$

where

$$Q(\eta) \stackrel{\text{def}}{=} \frac{\sinh \eta - \eta}{\sinh^3 \eta} (\cosh \eta + 1)^2. \quad (5.3)$$

The function $Q(\eta)$ has the following properties

$$Q(0) = 2/3, \quad \lim_{\eta \rightarrow \infty} Q(\eta) = 1, \quad (5.4)$$

$$\frac{dQ}{d\eta} > 0 \quad \text{for} \quad 0 < \eta < \infty. \quad (5.5)$$

The proof of (5.5) is given in the Appendix. Thus, Q is monotonic in its full range.

On the SCS, $r > r_{\text{sc}}$ must hold. The calculation stops at the r_{\max} given by (4.1) because $\mathcal{F}(r)$ is undetermined for $r > r_{\max}$. Consequently, for every $r \in (r_{\text{sc}}, r_{\max})$, (5.2) uniquely determines $\eta(r)$. Then, $t(r)$ along the SCS is calculated from (2.3):

$$t(r) = t_B + \frac{M_0}{(-k + \mathcal{F})^{3/2}} [\sinh \eta(r) - \eta(r)]. \quad (5.6)$$

From (5.2) one can see that at $r = r_{\text{sc}}$, where $E_{,r} = 0$, we have $Q = 1$, i.e. $\eta \rightarrow \infty$. Thus, the points of the SCS, at which $r = r_{\text{sc}}$, lie in the infinite future.

The profile of the SCS given by (5.6) is the upper \mathcal{U} -shaped curve in the right part of Fig. 3. The $t(r)$ on it decreases from $t = +\infty$ at $r = r_{\text{sc}}$ to

$$t = t_{\min} = 74.803824384008095 \text{ NTU} \quad (5.7)$$

achieved at

$$r = r_{\min} = 0.82084948116793433, \quad (5.8)$$

and then increases with increasing r up to the edge of the model given by (4.1). However, the numbers given in (5.7) and (5.8), which emerged while calculating the $t(r)$ from (5.6), are meaningful only up to the fourth decimal digit because of numerical fluctuations in the SCS profile. They are shown, in the vicinity of $r = r_{\min}$, in the inset in Fig. 3. The SCS has very large fluctuations for $r \rightarrow r_{\max}$, seen at the right margin of Fig. 3.

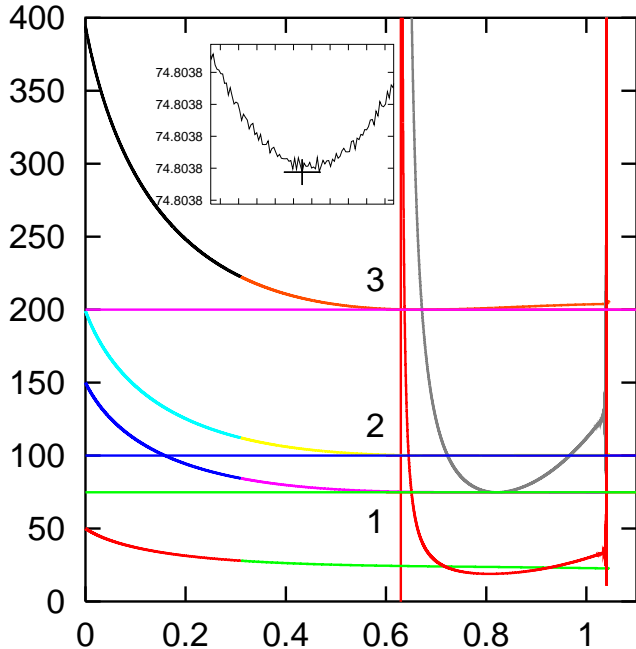


FIG. 3: **Main panel:** See text for explanations. **Inset:** The neighbourhood of $r = r_{\min}$ on the shell-crossing set. The cross marks the point $(r, t) = (r_{\min}, t_{\min})$ given by (5.7) and (5.8). The leftmost tic on the r -axis is at $r = 0.82076$, the rightmost one is at $r = 0.82094$, the tics are separated by $\Delta r = 2 \times 10^{-5}$.

Figure 3 shows the intersections of various hypersurfaces with a fixed 2-space of constant ϑ and φ . To get an idea about spatial relations, one should imagine Fig. 3 being rotated around the $r = 0$ axis – this would be the intersections of those hypersurfaces with the 3-space $\vartheta = \pi/2$.

The main panel of Fig. 3 shows several other curves that will be introduced in later sections. The lower \mathcal{U} -shaped curve is the extremum-redshift profile given by (10.2) – (10.3). The lowest of the other four curves is the profile of the light cone that hits the central observer at $t = 50$ NTU; it will become clear in Sec. IX why it is special. The remaining three curves are the profiles of the past light cones of the central observer that intersect the SCS at the times t_{\min} , t_2 and t_3 given by (5.7), (5.10) and (5.12). Note that all the light cones that intersect the SCS are horizontal at the intersection points. At the scale

of this figure, the light cone from Fig. 1 seems to coincide with the r -axis. The left vertical line marks $r = r_{\text{sc}}$, the right one is an artifact of numerical fluctuations as $r \rightarrow r_{\max}$. The horizontal lines 1, 2 and 3 mark the characteristic times explained below.

The time given by (5.7) can be written as

$$t_{\min} \approx 562.4T, \quad (5.9)$$

where T is given by (2.21). Thus, since the SCS lies far to the future of the light cone from Fig. 1, it has no influence on the past and present observations of the central observer. It will influence her observations beginning at $t = t_F$, where t_F is that instant, at which the light ray issued at $(r, t) = (r_{\min}, t_{\min})$ hits the center $r = 0$. The t_F will be determined in Sec. VIII.

The horizontal lines marked “1”, “2” and “3” in Fig. 3 are at those values of t , at which the profiles of density will be calculated in Sec. VI. The line marked “1”, is tangent to the SCS at $r = r_{\min}$. The line marked “2”, at

$$t = t_2 = 100 \text{ NTU}, \quad (5.10)$$

has two points of intersection with the SCS profile. The positions of those points can be read off from the table of values of $t(r)$ along the SCS, they are

$$r = r_{2a} \approx 0.722829 \quad \text{and} \quad r = r_{2b} \approx 0.967. \quad (5.11)$$

The line marked “3” intersects the SCS at one point, with the coordinates

$$t = t_3 = 200 \text{ NTU}, \quad r = r_3 \approx 0.671732. \quad (5.12)$$

VI. DENSITY DISTRIBUTIONS ON HYPERSURFACES OF CONSTANT t

We will now calculate the density distributions in our model along a few characteristic hypersurfaces. The curves in all the figures in this section have large numerical fluctuations at $r \rightarrow r_{\max}$ that look like vertical bars, these are ignored in the captions and explanations.

We first calculate the density at the time $t = 0$, where the light cone of Fig. 1 has its vertex. To this end, we use (2.2), (2.4), (3.2), (2.22) and $t = 0$ in (3.5) – (3.6) and in (3.1) to calculate $R(0, r)$ and $R_{,r}(0, r)$, then we substitute the results in (2.5). The resulting graph of $\kappa\rho(0, r)$ is shown in the main panel of Fig. 4. This is a void profile, in agreement with the conventional wisdom,³ but it has a cusp rather than a smooth minimum at the center.⁴ The hypersurface $t = 0$ does not intersect the SCS, so this

³ Many authors just reflexively use the term “void models” to denote L–T models mimicking accelerated expansion, see references in Refs. [9, 10]. In general, this is not correct – as demonstrated by the models of Refs. [9] and [1].

⁴ See footnote 1.

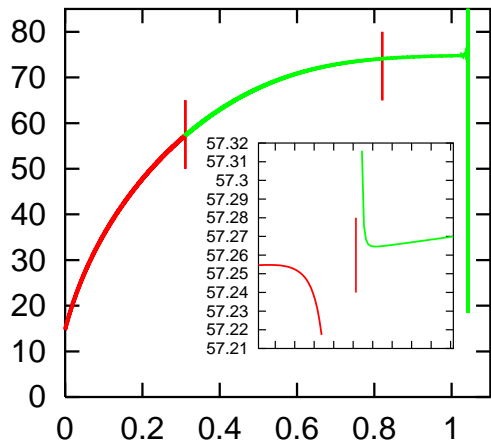


FIG. 4: **Main panel:** The mass density (2.5) calculated along the hypersurface $t = 0$ as a function of r . The quantity on the vertical axis is $\kappa\rho$, measured in $(\text{NLU})^{-2}$. The left vertical bar marks $r = r_{\text{AH}}$, the right one marks $r = r_{\text{sc}}$. **Inset:** Enlarged view of the neighbourhood of $r = r_{\text{AH}}$. The leftmost tic on the horizontal axis is at $r = 0.31046$, the rightmost tic is at $r = 0.31064$, the tics are separated by $\Delta r = 2 \times 10^{-5}$. The discontinuity is a consequence of numerical errors.

density is finite in the whole range. The inset in Fig. 4 shows an enlarged view of the neighbourhood of $r = r_{\text{AH}}$. The curve $\kappa\rho(0, r)$ has a discontinuity at $r = r_{\text{AH}}$ caused by numerical errors in calculating R and $R_{,r}$. These errors are consequences of inaccuracy in calculating $E(r)$ in the neighbourhood of $r = r_{\text{AH}}$, reported in Ref. [1].

The central density in this profile is

$$\kappa\rho(0, 0) = 14.837453949082986 (\text{NLU})^{-2}, \quad (6.1)$$

which corresponds to

$$\rho(0, 0) \approx 0.93 \times 10^{-30} \text{ g/cm}^3. \quad (6.2)$$

This is smaller than the present density in the ΛCDM model, which can be calculated⁵ from (2.12) using (2.10), (2.11) and (2.13):

$$\kappa\rho_0 \approx 43.075 (\text{NLU})^{-2}, \quad (6.3)$$

$$\rho_0 \approx 2.7 \times 10^{-30} \text{ g/cm}^3. \quad (6.4)$$

Figure 5 shows the graph of $\kappa\rho(t_{\text{min}}, r)$, where t_{min} is the time, given by (5.7), at which the hypersurface $t = t_{\text{min}}$ is tangent to the SCS at the $r = r_{\text{min}}$, given by (5.8). The density goes to infinity there, but stays positive for $r > r_{\text{min}}$. The main panel shows the position of the peak in density,⁶ the inset shows the values of $\kappa\rho$

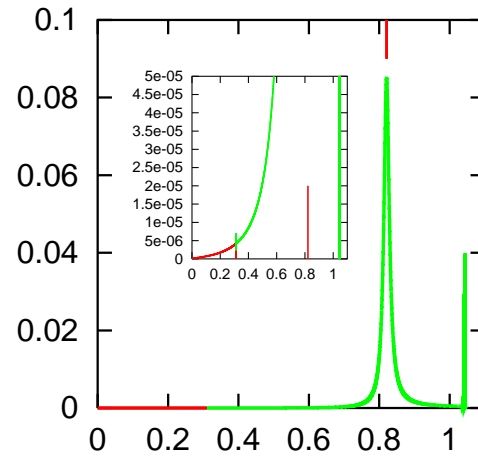


FIG. 5: **Main panel:** The mass density (2.5) calculated along the hypersurface $t = t_{\text{min}}$, given by (5.7), as a function of r . The units on the vertical axis are the same as in Fig. 4. The vertical bar at the top marks the value $r = r_{\text{min}}$, given by (5.8). **Inset:** Enlarged view of the neighbourhood of the r -axis. The right vertical bar marks $r = r_{\text{min}}$. What looks like another bar at $r = r_{\text{AH}}$ is a numerical fluctuation.

in a vicinity of the r -axis. The central density is

$$\begin{aligned} \kappa\rho(t_{\text{min}}, 0) &= 1.39237296085099607 \times 10^{-7} (\text{NLU})^{-2} \\ \implies \rho(t_{\text{min}}, 0) &\approx 8.73 \times 10^{-39} \text{ g/cm}^3. \end{aligned} \quad (6.5)$$

Figure 6 shows the graph of $\kappa\rho(t_2, r)$, where $t_2 = 100$ NTU. The hypersurface $t = t_2$ intersects the SCS at two values of r , given by (5.11). At $r \rightarrow r_{2a-}$, the density goes to $+\infty$ and becomes negative for $r > r_{2a}$. At $r \rightarrow r_{2b-}$, the density goes to $-\infty$ and becomes positive for $r > r_{2b}$. The main panel shows the peaks, the inset shows $\kappa\rho$ in a vicinity of the r -axis. The central density is

$$\begin{aligned} \kappa\rho(t_2, 0) &= 5.83260001345375805 \times 10^{-8} (\text{NLU})^{-2} \\ \implies \rho(t_2, 0) &\approx 3.66 \times 10^{-39} \text{ g/cm}^3. \end{aligned} \quad (6.6)$$

Figure 7 shows the graph of $\kappa\rho(t_3, r)$, where $t_3 = 200$ NTU. The hypersurface $t = t_3$ intersects the SCS at $r = r_3$, given by (5.12). At $r \rightarrow r_{3-}$, the density goes to $+\infty$ and becomes negative for $r > r_3$. The main panel shows the position of the peak in density, the inset shows $\kappa\rho$ in a vicinity of the r -axis. The central density is

$$\begin{aligned} \kappa\rho(t_3, 0) &= 7.29952961986280660 \times 10^{-9} (\text{NLU})^{-2} \\ \implies \rho(t_3, 0) &\approx 4.58 \times 10^{-40} \text{ g/cm}^3. \end{aligned} \quad (6.7)$$

The transitions between the situations shown in Figs. 4 – 7 occur in a nearly continuous way. At $t < t_{\text{min}}$, there is no singularity in $\rho(t, r)$. As $t \rightarrow t_{\text{min}-}$, the density at $r = r_{\text{min}}$ goes to infinity, but stays positive on both sides of r_{min} . When t increases above t_{min} , the two branches of $\rho(t, r)$ that go to $+\infty$ move sideways away from r_{min} , and a third branch appears that goes to $-\infty$ at $r \rightarrow r_{2a+}$

⁵ The conversion to g/cm^3 in (6.1) – (6.7) was done using (2.18) for the velocity of light and (2.24) for the gravitational constant.

⁶ Because of numerical inaccuracies, no point on the line $t = t_{\text{min}}$ actually coincides with any point on the SCS. Therefore, at $r = r_{\text{min}}$, the numerically calculated density becomes much larger than elsewhere, but is still finite.

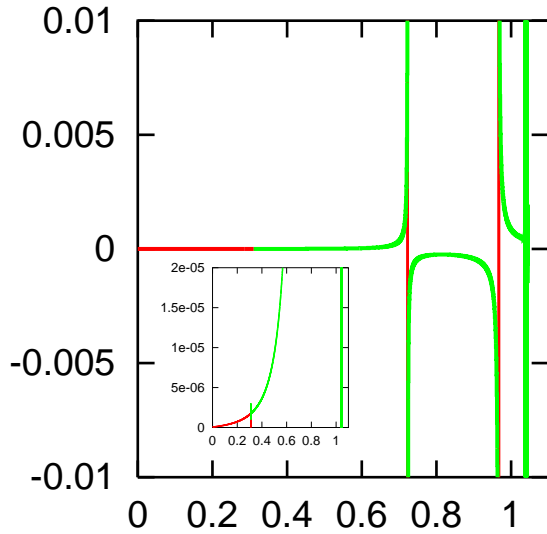


FIG. 6: **Main panel:** The mass density (2.5) as a function of r , calculated along the hypersurface $t = t_2 = 100$ NTU. The units on the vertical axis are the same as in Fig. 4. The vertical bars mark the values $r = r_{2a}$ and $r = r_{2b}$. **Inset:** Enlarged view of the neighbourhood of the r -axis. What looks like a vertical bar is a numerical fluctuation at $r = r_{AH}$.

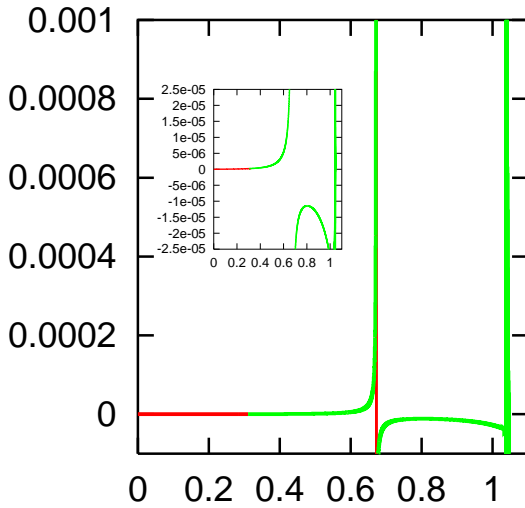


FIG. 7: **Main panel:** The mass density (2.5) as a function of r , calculated along the hypersurface $t = t_3 = 200$ NTU, which intersects the SCS at the value of r given by (5.12). The units on the vertical axis are the same as in Fig. 4. The vertical bar marks the value $r = r_3$. **Inset:** Enlarged view of the neighbourhood of the r -axis.

and $r \rightarrow r_{2b-}$. The situation in Fig. 7 does not really differ from that in Fig. 6; the second infinity in ρ has simply moved out of the region covered by our model.

VII. THE DENSITY DISTRIBUTION ALONG THE PAST LIGHT CONE OF THE PRESENT OBSERVER

The hypersurface $t = 0$ contains events simultaneous with $(t, r) = (0, 0)$, so the density distribution on it is unobservable at $(0, 0)$. The observable quantity is the density along the observer's past light cone. It was calculated from (2.5), where (2.4) was used for $M(r)$ and the numerical table for $R(t_{ng}(r), r)$ was taken from Ref. [1]. In calculating $R_{,r}(t_{ng}(r), r)$ from (3.1), eq. (3.2) was used for E , eq. (2.2) was used for $R_{,t}$, and the numerical tables for $\mathcal{F}(r)$ and $t_{ng}(r)$ were taken from Ref. [1]. In order to test the numerical accuracy, the calculation of $\kappa\rho(t_{ng}(r), r)$ in the range $r \in [0, r_{AH}]$ was carried out in two ways: forward from $r = 0$ and backward from $r = r_{AH}$, using the relevant tables for $t_{ng}(r)$ from Ref. [1]. Figure 8 shows $\kappa\rho(t_{ng}(r), r)$ in four separate views.

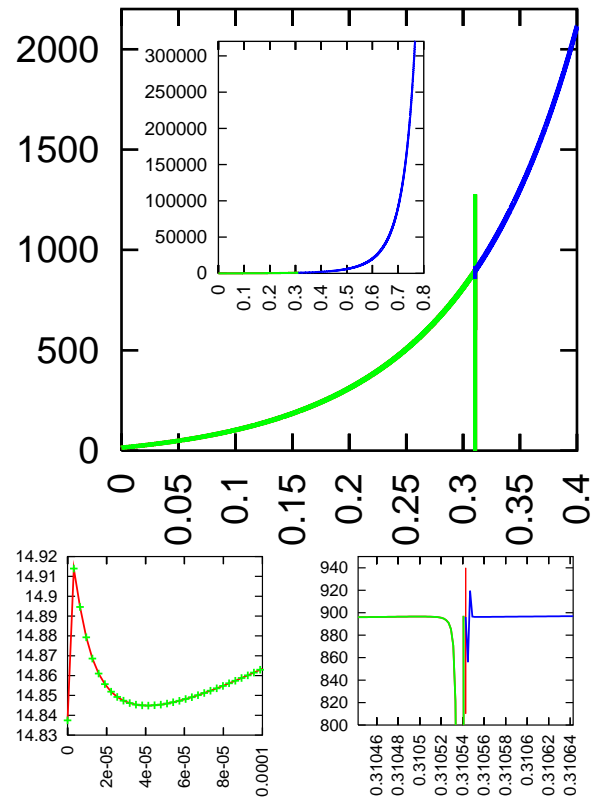


FIG. 8: The mass density (2.5) calculated along the light cone of Fig. 1 as a function of r . The units of $\kappa\rho$ are the same as in Fig. 4. See text for explanations.

The main panel shows the graph of $\kappa\rho$ in the range $r \in [0, 0.4]$. At $r = 0$, the value of $\kappa\rho$ is, of course, the same as in (6.1). What looks like a vertical bar is a numerical fluctuation at $r = r_{AH}$. The curves calculated forward from $r = 0$ and backward from $r = r_{AH}$ coincide perfectly, not only at this scale (see below).

The inset in the main panel shows the same graph

in the range $r \in [0, 0.8]$. With r approaching the r_{\max} given by (4.1), $\rho(t_{\text{ng}}(r), r)$ goes to infinity very fast. The numerical calculation broke down already at

$$r = r_{\text{bd}} = 1.0296253299989211, \quad (7.1)$$

with the largest value of $\kappa\rho$ yet calculated being

$$\kappa\rho_{\text{bd}} = 1.49073211697326822 \times 10^{18} \text{ (NLU)}^{-2}. \quad (7.2)$$

The lower left panel of Fig. 8 shows the neighbourhood of $r = 0$ and is meant to demonstrate that the curve calculated forward from $r = 0$ (the continuous line) agrees perfectly with the one calculated backward from $r = r_{\text{AH}}$ (the crosses) even at this scale. The fluctuation in the first step is inherited from the numerical calculation of $\mathcal{F}(r)$ in Ref. [1].

The lower right panel shows the neighbourhood of $r = r_{\text{AH}}$ (marked with the vertical bar), and the fluctuation, also inherited from $\mathcal{F}(r)$. Except for the segment $r \in [r_{\text{AH}} - \varepsilon, r_{\text{AH}} + \varepsilon]$, where $\varepsilon \approx 4 \times 10^{-5}$, the two parts of the graph fit together satisfactorily.

The numerical tables for $\kappa\rho(r)$ along the light cone, discussed above, and for $z(r)$, calculated in Ref. [1], were then combined to produce the table for $\kappa\rho(z)$. This does not differ in shape from $\kappa\rho(r)$, except that $z \rightarrow \infty$ at the BB, so the horizontal axis is stretched compared to that in Fig. 8. The graph of $\kappa\rho(z)$ is shown in Fig. 9. The segment $z \in [0, z_{\text{AH}}]$, where z_{AH} is given by (2.16), and the numerical fluctuation at z_{AH} , are squeezed into an invisible size. The right end of the z -axis is at $z = 1100$, which is close to the redshift at last scattering [22],

$$z_{\text{ls}} = 1089. \quad (7.3)$$

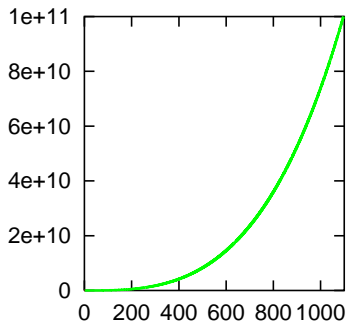


FIG. 9: The mass density (2.5) along the light cone of Fig. 1 as a function of z . The units of $\kappa\rho$ are the same as in Fig. 4.

VIII. THE FUTURE OBSERVATIONS OF THE SHELL CROSSINGS

As stated before, the SCS lies far to the future of the PCPO from Fig. 1. In order to find out, at what time the shell crossing will make itself seen for the central

observer, one must calculate the profile of that past light cone of the central observer that is tangent to the SCS at $(r, t) = (r_{\min}, t_{\min})$ given by (5.7) – (5.8). This was done by numerical fitting, and the result is the third curve from above in the left part of Fig. 3. It will reach the central observer at

$$t_F \approx 149.965 \text{ NTU} \approx 1063.58T, \quad (8.1)$$

where T is given by (2.21). This is the first instant, at which the central observer will get a signal from the SCS. See Sec. IX for more on this.

Since the equation of the SCS is $R_{,r} = 0$, Eq. (2.6) implies that a light ray intersecting the SCS must be horizontal in the (t, r) coordinates at the intersection point. The three uppermost rays in Fig. 3 illustrate this.

Let us now compare the travel times of two rays: one that is emitted at the BB and reaches the central observer at present ($t = 0$), and one that is emitted at the minimum of the SCS and reaches the central observer at $t = t_F$. The first time is given by (2.22), the second one is, from (5.7) and (8.1)

$$t_F - t_{\min} \approx 75.161 \text{ NTU}. \quad (8.2)$$

Thus $(t_F - t_{\min})/T_{\text{model}} \approx 565.12$, which may seem surprisingly large. A ray emitted from the minimum of the SCS proceeds from r_{\min} to the observer at $r = 0$, which seems to be only part of the way from r_{\max} given by (4.1) to $r = 0$, and yet the journey of the later-emitted ray lasts much longer than the present age of the Universe. This difference is a consequence of the illusion created by the comoving coordinates that we are using throughout this paper. The values of r are constant along the flow lines of the cosmic fluid and are not measures of distance from the symmetry center. Such a measure is, for example, $\int \frac{R_{,r} dr}{\sqrt{1+2E}}$ calculated at constant t . In consequence of expansion of the Universe, a particle at $r = r_{\min}$ is farther from the center at $t = t_{\min}$ than at any $t < t_{\min}$. Thus, the ray emitted from $r = r_{\min}$ at the t_{\min} given by (5.7) has a much larger distance to cover before reaching $r = 0$ than a ray emitted from the same r_{\min} at the BB, to reach the observer at $t = 0$.

IX. THE REDSHIFT PROFILES ALONG VARIOUS LIGHT CONES

It is interesting to trace the behaviour of redshift along various light rays. The profiles of $z(r)$ shown in Fig. 10 were calculated by solving (3.7) along the rays reaching the central observer at the times given below. The numbering begins at the upper edge of the figure from the left, and continues along the right edge from top to bottom.

1. $t = 0$ NTU. This is $z(r)$ along the ray emitted at the BB that reaches the central observer at present. It was calculated in Ref. [1] from the input data defining the model, and now re-calculated by solving (3.7). Tables I and II show the precision with

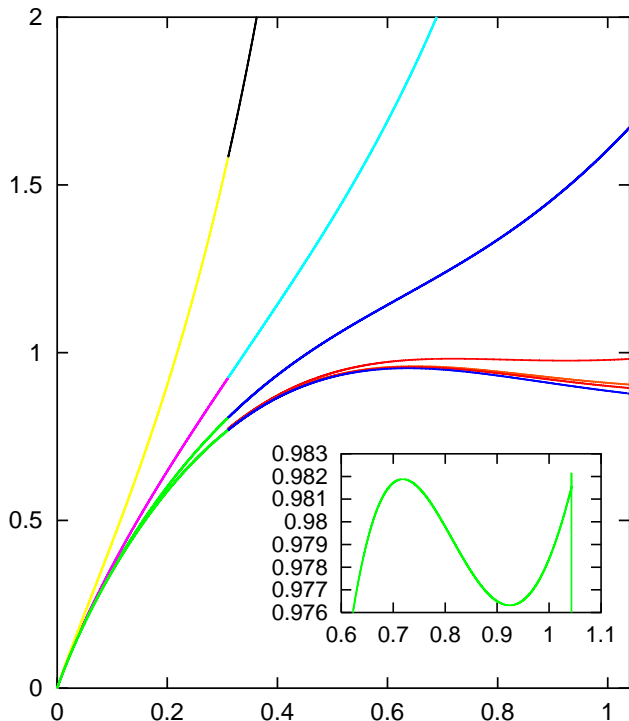


FIG. 10: Graphs of $z(r)$ along the rays reaching the central observer at various times from $t = 0$ NTU to $t \approx 394.3$ NTU. See text for details. **Inset:** Enlarged view of the right part of curve # 4 from the main graph. It clearly shows that $z(r)$ along this ray has a local maximum and a local minimum at (r, z) given by (9.1) and (9.2).

which the two results (dis-)agree. For Table II the initial values of r and z are given by (2.15) and (2.16). Wherever the difference is nonzero, the now-calculated $z(r)$ is greater.

2. $t = 1$ NTU.
3. $t = 5$ NTU.
4. $t = 50$ NTU. This ray and the next three are shown in Fig. 3.
5. $t \approx 149.965$ NTU. This is $z(r)$ along the ray emitted from the SCS at $(r, t) = (r_{\min}, t_{\min})$ given by (5.7) – (5.8).
6. $t \approx 199.083$ NTU. This is $z(r)$ along the ray that intersects the SCS at $t = t_2 = 100$ NTU.
7. $t \approx 394.314$ NTU. This is $z(r)$ along the ray that intersects the SCS at $t = t_3 = 200$ NTU.

A few facts about the graphs in Fig. 10 are noteworthy:

1. On curves # 1 to 3, $z(r)$ is monotonically increasing along the past light cones.
2. On curve # 4, whose corresponding light cone comes near the SCS, but does not intersect it (see Fig. 3 – this is the lowest of the four light cone profiles shown

TABLE I: Differences between the two $z(r)$ functions on ray 1 when (3.7) is integrated from $r = 0$

At	the difference is
r close to 0	0 (perfect agreement down to $\Delta r = 10^{-6}$)
r close to r_{AH}	$\Delta z = 1.2 \times 10^{-4}$
$r = 0.7$, where $z \approx 10.4$	$\Delta z = 2.7 \times 10^{-3}$
$r = 1.01$, where $z \approx 1050$	$\Delta z \approx 7$

TABLE II: Differences between the two $z(r)$ functions on ray 1 when (3.7) is integrated from $r = r_{\text{AH}}$

At	the difference is
r close to r_{AH}	0 (perfect agreement down to $\Delta r = 10^{-6}$)
$r = 0.7$	$\Delta z = 2.2 \times 10^{-3}$
$r = 1.01$	$\Delta z \approx 3.8$

there), $z(r)$ goes through a maximum and then through a minimum before the ray escapes through the edge of the model. The coordinates of these extrema are

$$\begin{pmatrix} r \\ z \end{pmatrix}_{4\text{max}} = \begin{pmatrix} 0.71831446207852601 \\ 0.98188047082901109 \end{pmatrix}, \quad (9.1)$$

$$\begin{pmatrix} r \\ z \end{pmatrix}_{4\text{min}} = \begin{pmatrix} 0.92427265264269520 \\ 0.97631849413594207 \end{pmatrix}. \quad (9.2)$$

3. On curves # 6 to 8, $z(r)$ goes through a maximum, and then keeps decreasing up to the edge of the model given by (4.3). The coordinates of these maxima are:

$$\begin{pmatrix} r \\ z \end{pmatrix}_{5\text{max}} = \begin{pmatrix} 0.65078589679780396 \\ 0.95958866411532251 \end{pmatrix}, \quad (9.3)$$

$$\begin{pmatrix} r \\ z \end{pmatrix}_{6\text{max}} = \begin{pmatrix} 0.64511331512911863 \\ 0.95709853786786281 \end{pmatrix}, \quad (9.4)$$

$$\begin{pmatrix} r \\ z \end{pmatrix}_{7\text{max}} = \begin{pmatrix} 0.63704541339084608 \\ 0.95340148625320642 \end{pmatrix}. \quad (9.5)$$

These maxima *do not* occur at the intersections of the corresponding light cones with the SCS. At the SCS, $z(r)$ is already decreasing, which means that light passing near an SCS acquires local blueshifts. The redshift profiles remain smooth at those intersections and do not display any special behaviour there.

X. THE EXTREMUM-REDSHIFT HYPERSURFACE

Figure 10 shows that on the light cones that come near to the SCS, the redshift begins to decrease on approaching the SCS, and, at the intersection of the light cone with the SCS, $dz/dr < 0$. Thus, light emitted close to the SCS displays local blueshifts, and this is an analogy to the behaviour of light in a vicinity of a nonconstant BB [17, 18], [14]. The difference is that blueshifts generated at the nonconstant BB are seen as infinite by all later observers, while those generated at the SCS are finite, and, as the graphs in Fig. 10 demonstrate, are swamped with excess by redshifts built up later if the observer is far enough to the future. The central observer sees the light from the SCS being redshifted.

The location of the hypersurface, at which blueshifts go over into redshifts along radial rays, is observer-independent and can be calculated from (2.7). At that hypersurface, which we will call the extremum-redshift hypersurface, we have $dz/dr = 0$, so $R_{,tr} = 0$. We find from (3.11):

$$R_{,tr} = \left[\sqrt{-k + \mathcal{F}} + \frac{r\mathcal{F}_{,r}}{2\sqrt{-k + \mathcal{F}}} \right] \frac{\sinh \eta}{\cosh \eta - 1} - \frac{3}{2} \frac{r\mathcal{F}_{,r}}{\sqrt{-k + \mathcal{F}}} \frac{\sinh \eta - \eta}{(\cosh \eta - 1)^2}. \quad (10.1)$$

For numerical solving, the equation $R_{,tr} = 0$ can be written in a form similar to (5.2) – (5.3):

$$\frac{1}{r} + \frac{\mathcal{F}_{,r}}{2(-k + \mathcal{F})} [1 - 3P(\eta)] = 0, \quad (10.2)$$

where

$$P(\eta) \stackrel{\text{def}}{=} \frac{\sinh \eta - \eta}{\sinh \eta (\cosh \eta - 1)}. \quad (10.3)$$

We have $P(0) = 1/3$, $\lim_{\eta \rightarrow \infty} P(\eta) = 0$ and $dP/d\eta < 0$ for all $\eta > 0$. Hence, $P(\eta)$ is monotonic in the full range of η , and, if a solution of (10.2) exists, then it is unique.

Having found η for a given r , we then calculate $t(r)$ on the ERH from (5.6). The profile of the ERH is the lower \mathcal{U} -shaped curve in Fig. 3.

Using (5.2) to eliminate $\mathcal{F}_{,r}$, we find that at the SCS

$$R_{,tr} = -\frac{3}{2} \frac{\sqrt{-k + \mathcal{F}}(\eta \cosh \eta + 2\eta - 3 \sinh \eta)}{(\cosh \eta - 1)^2 (\frac{3}{2}Q - 1)}. \quad (10.4)$$

By (5.4) – (5.5) we have $\frac{3}{2}Q - 1 > 0$ for all $\eta > 0$, and it is easy to verify that also $\eta \cosh \eta + 2\eta - 3 \sinh \eta > 0$ for all $\eta > 0$. Therefore (10.4) shows that $R_{,tr} < 0$ at the intersection of a radial light ray with the SCS, which, using (2.7), means $dz/dr < 0$. Hence, light emitted from the SCS is blueshifted in a vicinity of the emission point. But the $R_{,tr}$ given by (10.4) is finite at all $\eta > 0$ (including $\eta \rightarrow \infty$, where $R_{,tr} = 0$), so the blueshift is also finite.

The points on the light-cone profiles that correspond to the extrema in z listed in (9.1) – (9.5) should all lie on

the ERH. They do, but with a rather modest numerical precision. The t -coordinates of the points on the ERH are smaller than the corresponding t -s on the light cones by ≈ 0.13 NTU in the case of both extrema on curve # 4 and of the maximum on curve #7, and by ≈ 0.14 NTU in the other two cases.

We called the hypersurface given by (10.2) – (10.3) an extremum (rather than maximum) redshift hypersurface because, as seen from Fig. 10, on ray # 4 that intersects this hypersurface twice, the redshift profile has a maximum at one intersection point and a minimum at the other. Generally, redshift profiles have maxima on the “inside” branch of the ERH (the one closer to the center) and minima on the “outside” branch. On a ray tangent to the ERH, the redshift profile has an inflection at the point of tangency.

The appearance of local blueshifts is a signal that the ray (followed back in time) is approaching the SCS. However, the blueshifts, being only local and being overcompensated by redshifts along the later part of the ray, may not be noticed by the future central observer, unless she is able to determine the location of the light signal along the light cone independently of the value of z , and with a sufficient precision. But even if she is, the precise moment of crossing the SCS leaves no recognizable mark in the redshift profile – $z(r)$ is smooth at the intersection of the ray with the SCS.

Note also that there are local blueshifts on curve # 4 in Fig. 10, even though the corresponding ray never intersects the SCS – it just passes nearby. So, locating an SCS by observations is going to be a difficult problem.

XI. THE $D_A(z)$ AND $D_L(z)$ RELATIONS ON RAYS INTERSECTING THE ERH

Quantities that are in principle observable, like the angular diameter distance from the central observer D_A (which is equal to the function $R(t_{\text{ng}}(r), r)$ appearing in (2.8)) or the luminosity distance from the central observer D_L (given by (2.8)), are usually expressed as functions of redshift. The peculiar behaviour of redshift on rays passing near the SCS ($z(r)$ being non-monotonic) causes an even more peculiar behaviour of $D_A(z)$ and $D_L(z)$: where $z(r)$ is not monotonic, the relations $D_A(z)$ and $D_L(z)$ fail to be single-valued (and therefore cannot be called functions). This is illustrated in Figs. 11 and 12 that show these two relations along rays # 4 and 7 from Fig. 10. Along ray # 4 in the neighbourhood of the SCS, three values of D_A and three values of D_L correspond to a single value of z . Along ray # 7 in the neighbourhood of the SCS, the relations $D_A(z)$ and $D_L(z)$ become double-valued.

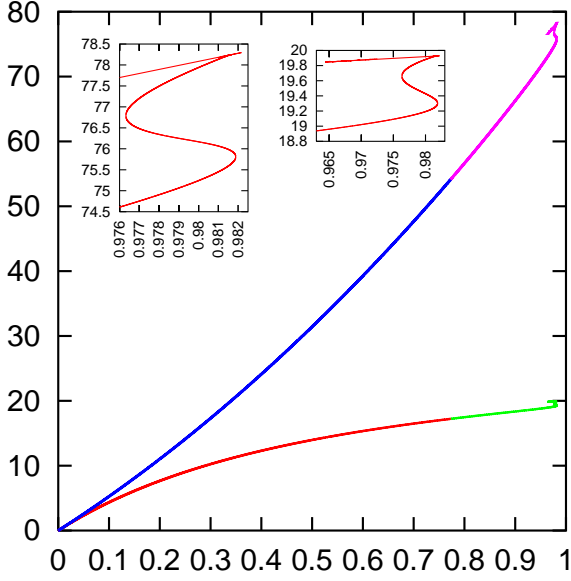


FIG. 11: **Main panel:** The relations $D_A(z)$ (lower curve) and $D_L(z)$ (upper curve) along ray # 4 from Fig. 10 (this is the lowest ray in Fig. 3 that intersects the extremum-redshift profile twice). **Insets:** The upper ends of the curves from the main panel, where the relations $D_L(z)$ (left inset) and $D_A(z)$ (right inset) become triple-valued. The nearly straight segments at the upper edges of the graphs are numerical fluctuations at the edge of the model.

XII. THE RECOMBINATION EPOCH

It is interesting to compare some of the characteristics of the model discussed here with those of the Λ CDM model. The metric of the Λ CDM model is [1]

$$ds^2 = dt^2 - S^2(t) [dr^2 + r^2(d\vartheta^2 + \sin^2 \vartheta d\varphi^2)] \quad (12.1)$$

with

$$S(t) = \left(-\frac{6M_0}{\Lambda} \right)^{1/3} \sinh^{2/3} \left[\frac{\sqrt{-3\Lambda}}{2} (t - t_{B\Lambda}) \right], \quad (12.2)$$

where $M_0 = 1$ NLU, t_B is given by (2.22), and Λ is calculated from (2.10) – (2.13), (2.18) and (2.24) to be

$$-\Lambda = 3\Omega_\Lambda H_0^2 = 91.849164 \text{ (NLU)}^{-2}. \quad (12.3)$$

We assume

$$t_{\text{rec}} - t_B = 3.8 \times 10^5 y = 3.88 \times 10^{-6} \text{ NTU} \quad (12.4)$$

for the time of last scattering [23]⁷ in the Λ CDM model.

⁷ In fact, the last scattering was not an instant strictly localizable in time, but a process that lasted some time (see e.g. Ref. [24]). However, most astrophysical papers do not take this into account.

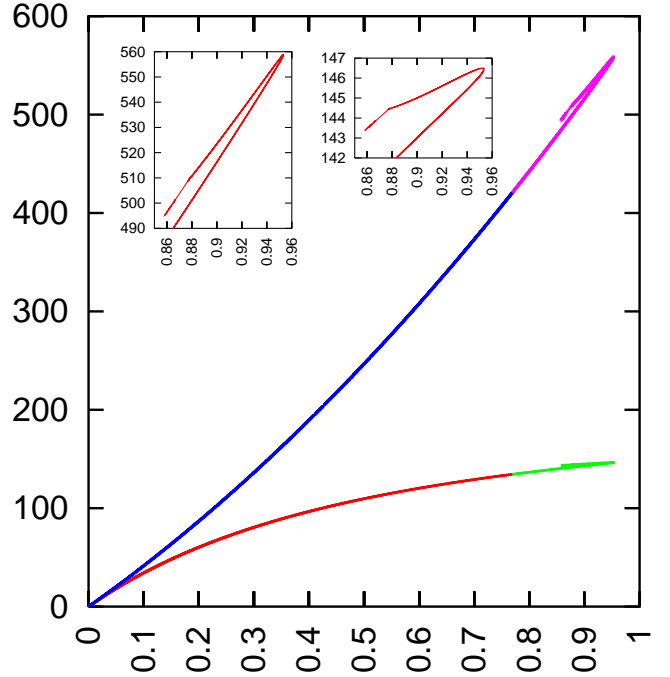


FIG. 12: The analogue of Fig. 11 along ray # 7 from Fig. 10 (this is the highest ray in Fig. 3). Now the relations $D_L(z)$ and $D_A(z)$ become double-valued close to the shell crossing.

The mass density in all $p = 0$ RW models obeys [14]

$$\kappa\rho = C_0/S^3(t), \quad (12.5)$$

where C_0 is a constant. Therefore, taking (6.4) for the present mass density, (2.21) for the current value of $t - t_B$, and (12.4) for the value of $t - t_B$ at last scattering, we calculate the mass density ρ_{ls} at last scattering to be

$$\begin{aligned} \kappa\rho_{\text{ls}} &= \kappa\rho_0 \frac{S^3(T)}{S^3(t_{\text{rec}} - t_B)} \\ &= 88089589221.4818 \approx 88 \times 10^9 \text{ (NLU)}^{-2}. \end{aligned} \quad (12.6)$$

We will now assume that the last scattering in the L–T model occurs at the same density; the last scattering time will thus depend on r . This is an approximate method of determining $(t_{\text{rec}} - t_B)$; for a more precise method see Refs. [25] and [26].

A density approximately equal to (12.6),⁸ namely

$$\kappa\rho_{\text{LTLS}} = 88017457848.852432, \quad (12.7)$$

is attained along the PCPO at the redshift

$$z_{\text{LTLS}} = 1054.891484271654, \quad (12.8)$$

⁸ The values that follow were read off from the numerical tables used to draw the figures in this paper.

not much different from (7.3). This happens at

$$r_{\text{LTLS}} = 1.010092188377007, \quad (12.9)$$

and this corresponds to the time along the PCPO

$$t_{\text{LTLS}} = -0.1329399592464457, \quad (12.10)$$

which is later than the BB by

$$\tau = 3.3614380286 \times 10^{-6} \text{ NTU} \approx 3.2942 \times 10^5 \text{ y.} \quad (12.11)$$

The difference between (12.11) and (12.4) has a simple intuitive explanation (see Fig. 13, copied from Ref. [1]). In any L–T model, every constant- r shell evolves by eq. (2.2), which is the same as the Friedmann equation, except that here $E(r)$ is different for every shell, and so is $M(r)$. The Friedmann curvature index k_F is related to E by $2E = -k_F r^2$, so, by (3.2), we have

$$k_F(r) = k - \mathcal{F}(r), \quad (12.12)$$

i.e. it is different for every shell. As Fig. 13 shows, $|k_F|$ is largest at $r = 0$ and monotonically decreasing, so the matter shells closer to $r = 0$ expand according to a “faster” Friedmann equation than the more distant ones. Also, they expand faster than the corresponding Λ CDM shells, as can be seen by comparing (2.21) with (2.22) and (6.1) with (6.3): the central region of the L–T model produced a lower density than Λ CDM in a shorter time. Consequently, the density required for recombination must have been achieved in a shorter time, too.

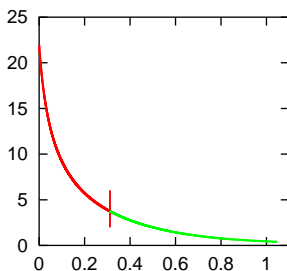


FIG. 13: Graph of the function $(-k_F(r)) \equiv |-k + \mathcal{F}|$. The vertical stroke is at $r = r_{\text{AH}}$.

XIII. FINAL SUMMARY

The L–T model considered here duplicates the luminosity distance vs. redshift relation $D_L(z)$ of the Λ CDM model using the energy function $E(r)$ alone. Its existence was proved first in Ref. [4], and then, by a more precise method, in Ref. [5]. It was explicitly (numerically) constructed in Refs. [5] and (in different coordinates) [1]. It turned out that this model necessarily contains a region where shell crossings occur [1]. This region is far enough from the central observer to cause no problems with the

interpretation of observations of the type Ia supernovae – its inner boundary intersects the past light cone of the present observer at $z \approx 6.9$. Therefore, it can be removed from the spacetime by matching the L–T model to a Friedmann background, without harming the usability of the model for explaining the $D_L(z)$ function. This much was proven in Ref. [1].

Here, the consequences of existence of the shell crossings were investigated. They are interesting from the point of view of geometry. They might become meaningful also for cosmology if a qualitatively similar model with different numerical parameters emerges from some other research. In such a model, the SCS might appear early enough to be visible for the present observer.

The model extends from the center of symmetry up to a finite distance (Sec. IV). The edge of the model is formed by the world lines of those cosmic matter particles that were ejected from the Big Bang at its contact with the past light cone of the present central observer. The model can be extended by matching it to either another L–T model or to a Friedmann model, but the extensions are arbitrary – they are not constrained by the $D_L(z)$ relation that defined our model, and were not considered in this paper.

The earliest point of the shell-crossing set is at $t = t_{\text{min}} \approx 74.8 \text{ NTU} \approx 562.4T$ to the future from now, where $T = 13.819 \times 10^9 \text{ y} = 0.141 \text{ NTU}$ is the present age of the Universe (Sec. V). The signal sent from that point would reach the central observer at $t_F \approx 149.965 \text{ NTU} \approx 1063.58T$ to the future from now (Sec. VIII).

Mass density distributions along a few hypersurfaces of constant t , and along the past light cone of the present central observer were numerically calculated (Secs. VI and VII). As expected, the density goes to infinity whenever such a hypersurface touches or intersects the SCS.

Characteristic examples of light rays that intersect the SCS were calculated (Sec. VIII). As expected, in the comoving coordinates they are horizontal at the intersection points. Then, redshift profiles along several light rays were calculated, including those mentioned above (Sec. IX). It turned out that on rays passing near the SCS, redshift acquires a maximum *before* the ray crosses the SCS, and at the intersection with the SCS the function $z(r)$ is already decreasing. It is surprising that the intersection with the SCS leaves no recognizable trace in the redshift profile: it is smooth there, and has no extremum. Thus, an observer placed down a light cone from the SCS would not notice any sign of the mass density being infinite there.

The extremum-redshift hypersurface, on which the redshift profiles acquire maxima and minima, was determined in Sec. X. Rays that cross the ERH display local blueshifts on the other side of it. In particular, they are blueshifted when emitted at the SCS. However, the blueshifts are finite, and become overcompensated by redshifts before the ray reaches the central observer.

The relations $D_A(z)$ and $D_L(z)$ along two rays (one passing near, the other crossing the SCS) were displayed

in Sec. XI (D_A is the angular diameter distance and D_L is the luminosity distance from the central observer). In consequence of the blueshifts generated in a vicinity of the SCS, these relations become double- or triple-valued near the SCS.

Finally, the end-instant of the recombination epoch along the radial ray reaching the central observer at present was calculated for the model considered here. It occurs at $t \approx 3.29 \times 10^5$ y after the Big Bang, vs. 3.8×10^5 y in the Λ CDM model. The difference finds a simple explanation in the profile of the $E(r)$ function; details are given in Sec. XII.

It is hoped that the investigation presented here will be useful if a model with a shell crossing within the view of the present observer emerges from some future research.

Appendix: The proof of (5.5)

The function $Q(\eta)$ of (5.5) can be written as

$$Q(x) = \frac{\cosh^2 x}{\sinh^2 x} - \frac{x \cosh x}{\sinh^3 x}, \quad \text{where } x \stackrel{\text{def}}{=} \eta/2. \quad (\text{A.1})$$

Then

$$\frac{dQ}{dx} = \frac{L(x)}{\sinh^4 x}, \quad (\text{A.2})$$

where

$$L(x) \stackrel{\text{def}}{=} -3 \sinh x \cosh x + 2x \sinh^2 x + 3x. \quad (\text{A.3})$$

The $L(x)$ has the following properties

$$L(0) = 0, \quad (\text{A.4})$$

$$dL/dx = -3 \cosh^2 x - \sinh^2 x + 4x \sinh x \cosh x + 3, \quad (\text{A.5})$$

$$(dL/dx)(0) = 0, \quad (\text{A.6})$$

$$d^2L/dx^2 = -4 \sinh x \cosh x + 4x(\sinh^2 x + \cosh^2 x), \quad (\text{A.7})$$

$$(d^2L/dx^2)(0) = 0, \quad (\text{A.8})$$

$$d^3L/dx^3 = 16 \sinh x \cosh x > 0 \quad \text{for all } x > 0. \quad (\text{A.9})$$

Equations (A.4) – (A.9) considered in reverse order imply that $L(x) > 0$ for all $x > 0$, so $dQ/d\eta = 2dQ/dx > 0$ for all $\eta > 0$. \square

Acknowledgements I am grateful to Jim Zibin for an insightful remark, and to the referee for comments that inspired an extension of the first version of this paper.

-
- [1] A. Krasinski, *Phys. Rev.* **D90**, 023524 (2014).
[2] G. Lemaître, *Ann. Soc. Sci. Bruxelles* **A53**, 51 (1933); English translation (as a Golden Oldie): *Gen. Relativ. Gravit.* **29**, 637 (1997).
[3] R. C. Tolman, *Proc. Nat. Acad. Sci. USA* **20**, 169 (1934); reprinted as a Golden Oldie: *Gen. Relativ. Gravit.* **29**, 931 (1997).
[4] H. Iguchi, T. Nakamura and K. Nakao, *Progr. Theor. Phys.* **108**, 809 (2002).
[5] C.-M. Yoo, T. Kai and K. Nakao, *Progr. Theor. Phys.* **120**, 937 (2008).
[6] A. G. Riess *et al.*, *Astron. J.* **116**, 1009 (1998).
[7] S. Perlmutter *et al.*, *Astrophys. J.* **517**, 565 (1999).
[8] D. O. Jones *et al.*, *Astrophys. J.* **768**, 166 (2013).
[9] M.-N. Célérier, K. Bolejko and A. Krasinski, *Astronomy and Astrophysics* **518**, A21 (2010).
[10] K. Bolejko, M.-N. Célérier and A. Krasinski, *Class. Quant. Grav.* **28**, 164002 (2011).
[11] R. A. Vanderveld, E. E. Flanagan and I. Wasserman, *Phys. Rev.* **D74**, 023506 (2006).
[12] A. Krasinski, C. Hellaby, K. Bolejko and M.-N. Célérier, *Gen. Rel. Grav.* **42**, 2453 (2010).
[13] Planck collaboration, *Planck* 2013 results. XVI. Cosmological parameters. arXiv:1303.5076; accepted for *Astronomy and Astrophysics*
[14] J. Plebański and A. Krasinski, *An Introduction to General Relativity and Cosmology*. Cambridge University Press 2006, 534 pp, ISBN 0-521-85623-X.
[15] A. Krasinski, *Inhomogeneous Cosmological Models*, Cambridge University Press 1997, 317 pp, ISBN 0 521 48180 5.
[16] H. Bondi, *Mon. Not. Roy. Astr. Soc.* **107**, 410 (1947); reprinted as a Golden Oldie in *Gen. Relativ. Gravit.* **31**, 1777 (1999).
[17] P. Szekeres, in: *Gravitational Radiation, Collapsed Objects and Exact Solutions*. Edited by C. Edwards. Springer (Lecture Notes in Physics, vol. 124), New York, pp. 477 – 487 (1980).
[18] C. Hellaby and K. Lake, *Astrophys. J.* **282**, 1 (1984) + erratum *Astrophys. J.* **294**, 702 (1985).
[19] A. Krasinski, *Phys. Rev.* **D89**, 023520 (2014) + erratum *Phys. Rev.* **D89**, 089901(E) (2014).
[20] <http://www.asknumbers.com/LengthConversion.aspx>
[21] http://www.physics.nist.gov/cgi-bin/cuu/Value?bg|search_for=unive
[22] M. Luciuk, *Astronomical Redshift*, <http://www.asterism.org/tutorials/tut29-1.htm>, last updated 2004.
[23] <http://astronomy.swin.edu.au/cosmos/e/epoch+of+recombination>
[24] K. Bolejko, *Mon. Not. R. Astron. Soc.* **370**, 924 (2006).
[25] C.-M. Yoo, K.-i. Nakao and M. Sasaki, *Journal of Cosmology and Astroparticle Physics* **1007(2010)**, 012 (2010).
[26] C.-M. Yoo, K.-i. Nakao and M. Sasaki, *Journal of Cosmology and Astroparticle Physics* **1010(2010)**, 011 (2010).